

Approaches to Autonomous Aerobraking at Mars

by

Jill Lynette Hanna
B.A. in Physics
June 1999, Northwestern University

A Thesis submitted to

The Faculty of
The School of Engineering and Applied Science

of The George Washington University in partial satisfaction
of the requirements for the degree of Master of Science

January 31, 2002

Thesis directed by
Robert H. Tolson

This research was conducted at NASA Langley Research Center

Abstract

Planetary atmospheric aerobraking was first performed during the extended part of the Magellan mission to Venus. The technique proved so efficient at providing significant reductions in orbital energy without major propulsive utilization, that it was designed for the Mars Global Surveyor (MGS) mission. The technique was planned for the failed Mars 1998 Polar Orbiter mission, will be utilized for the Mars 2001 Odyssey mission, and will most likely be incorporated in the future Mars Reconnaissance Orbiter mission. For all of these missions, aerobraking requires an intensive workforce during operations. At Mars, orbit to orbit variations in atmospheric density at aerobraking altitudes proved to have as large as a 35% standard deviation, which results in large variations in aeroheating. To provide safe and efficient aerobraking, both navigation and spacecraft system teams must be extremely diligent in updating spacecraft sequences and performing periapsis raise or lower maneuvers.

Automating the process with onboard measurements could significantly reduce the operational burden and, in addition, could reduce the potential for human error. Two levels of automation are presented and validated using part of the MGS aerobraking sequence and a simulated Mars Odyssey sequence. The simplest method only provides the capability to update the onboard sequence. This method utilizes onboard accelerometer measurements to estimate the change in orbital period during an aerobraking pass and thereby estimates the beginning of the next aerobraking sequence. Evaluation of the method utilizing MGS accelerometer data showed that the time of the next periapsis can be estimated to within a standard deviation of 8% of the change in the

orbital period due to drag. The second approach provides complete onboard orbit propagation. A low order gravity model is proposed that is sufficient to provide periapsis altitude predictions to within 100-200 meters over 3 orbits. Accelerometer measurements are used as part of the trajectory force model while the spacecraft is in the atmosphere.

Acknowledgements

The author would like to thank Dr. Robert Tolson for his time and effort in advising this thesis. She would also like to thank her committee members, Dr. John Whitesides, Dr. Mary Kae Lockwood, and Dr. Robert Tolson, for their thorough examination of the effort brought henceforth. A special note of appreciation is extended to Mr. Ben George for his assistance in the gravity field model, to Ms. Alicia Dwyer for assistance in implementation of an atmospheric wave model, and to Ms. Michelle Munk and Mr. Paul Tartabini for additional help in her analysis. This research was supported by the Jet Propulsion Laboratory under Contract 1213940.

Table of Contents

Abstract.....	ii
Acknowledgements.....	iv
Table of Contents.....	v
List of Figures.....	vii
Nomenclature.....	ix
Introduction.....	1
1. Level 1 of Autonomous Aerobraking.....	6
1.1 Method 1-- ΔV Impulse at Periapsis.....	6
1.2 Method 2—Complete Integration of Accelerometer Measurements.....	9
1.3 Results of Level 1.....	11
2. Level 2 of Autonomous Aerobraking.....	13
2.1 Gravity Field.....	13
2.2 Validation of Numerical Integration Scheme.....	15
2.3 Minimum Size Low Order Gravity Field.....	17
2.4 Analytic Perturbations.....	20
2.5 Trajectory Model Implications.....	21
2.6 Atmospheric Model.....	23
2.7 Maneuver Strategy.....	25
2.8 Typical Mission Simulation.....	28
2.9 Effects of Corridor Variation.....	30
2.10 Dust Storm Mission Simulation.....	34
Concluding Remarks.....	37

References..... 39

Appendix A. Sample OPTG File 40

Appendix B. Atmospheric Wave Model..... 42

List of Figures

Figure 1. Typical sequence of events for MGS	3
Figure 2. Period change difference between method 1 and radio tracking data.....	9
Figure 3. Prediction error in period change between complete integration (method 2) and radio tracking data.....	10
Figure 4. Prediction error in period change between complete integration (method 2) and radio tracking data.....	11
Figure 5. Difference in periapsis distance and time of periapsis between POST 20 by 20 gravity field and RK integration 20 by 20 gravity field.....	16
Figure 6. Maximum difference in periapsis distance and time of periapsis passage between a 20 by 20 gravity field and a 3 by 3 gravity field.....	18
Figure 7. Maximum difference in periapsis distance and time of periapsis passage between a 20 by 20 gravity field and a 4 by 4 gravity field.....	19
Figure 8. Maximum difference in periapsis distance and time of periapsis passage between a 20 by 20 gravity field and a 5 by 5 gravity field.....	20
Figure 9. Forty orbits integrated with a 4 by 4 gravity field and drag.....	22
Figure 10. Density in northern hemisphere from thermosphere model.....	24
Figure 11. Scale height in northern hemisphere from thermosphere model.....	24
Figure 12. Maneuver corridor.....	27
Figure 13. Maneuver related parameters for a typical maneuver strategy.....	29
Figure 14. Orbit parameter evolution for a typical maneuver strategy.....	30
Figure 15. Maneuver strategy 1	31
Figure 16. Maneuver strategy 2.....	32

Figure 17. Maneuver strategy 3.	33
Figure 18. Maneuver strategy 4.	34
Figure 19. Maneuver parameters for the dust storm case.	36

Nomenclature*

a	semi-major axis
a_T	tangential acceleration
e	eccentricity
inc	inclination
h	altitude
J_2	second zonal harmonic
J_3	third zonal harmonic
MGS	Mars Global Surveyor
Nq	Nyquist, 1 sample per second
OPTG	Orbit Propagation Trajectory Generation
p	semi-latus rectum
P	orbit period
Q	heat flux
r	spacecraft position
r_p	periapsis distance
R	reference radius
RK	Runge-Kutta integration
s/c	spacecraft
sol	one Mars day, 24 hours and 37 minutes
v	spacecraft velocity
v_m	maneuver velocity

* Unless otherwise noted, all units are in kilometers, kilograms, and seconds

v_p	s/c velocity at periapsis
Δv	change in velocity over time
ΔV	instantaneous change in velocity, typically due to maneuver
λ	longitude
μ	gravitational constant of Mars
ρ	atmospheric density
σ	standard deviation
τ	time of periapsis passage
φ	geocentric latitude
ω	argument of periapsis
Ω	longitude of ascending node

Introduction

Atmospheric aerobraking has been used in two planetary missions to change an elliptical orbit to a nearly circular orbit. The Magellan mission to Venus accomplished aerobraking after the science mission had been completed such that aerobraking could be demonstrated without being a mission critical operation.¹ The atmosphere of Venus is benign and repeatable mainly because the planet rotates slowly. The spacecraft was not designed for aerobraking, but because of the absence of orbit-to-orbit variability in atmospheric density, the aerobraking phase of the mission was a relatively uneventful success.

The success of Magellan aerobraking proved that ΔV could be significantly reduced using aerobraking, and aerobraking was selected as an enabling technology for the Mars Global Surveyor (MGS) mission. Unlike Magellan, for MGS aerobraking was critical to mission success, and MGS was the first planetary spacecraft designed for an aerobraking mission. The preflight estimate of atmospheric orbit to orbit variability had a standard deviation of 35%, and this estimate was subsequently verified during the mission.² Since the spacecraft thermal margin was set at 90% of the flight allowable limit, aerobraking MGS required intensive analysis and human interaction during operations to make maneuver decisions. The determining factor in implementing a maneuver for both spacecraft was heating. The solar arrays of both Magellan and MGS were the main drag surfaces of the spacecraft and the maximum temperature of the adhesives used in the solar arrays was the limiting factor. However, due to the damaged MGS solar array, the

aerodynamic moment placed on the solar array became the limiting factor at about $\frac{1}{2}$ the dynamic pressure that would have been seen if nominal aerobraking had taken place.²

For each orbit about Mars, a sequence of events was completed for MGS to prepare for entry into the Martian atmosphere. A typical sequence, shown in Figure 1, included at least the following actions:

1. Turn on catalyst bed heaters. This warms the thrusters to minimize damage to the spacecraft
2. Maneuver into aerobraking attitude and configure s/c for aerobraking. The aerobraking configuration minimizes the effects of aerodynamic torques on the spacecraft.
3. Discontinue operation of the communication system and begin recording engineering data. The high gain antenna usually does not point at the Earth in the aerobraking orientation.
4. Switch from reaction wheel control to thruster control. Because of the large aerodynamic moments, the base line reaction wheels could not provide enough torque to control the s/c while in the atmosphere
5. Increase attitude control dead band. Because the s/c was longitudinally aerodynamically stable, control was required only for excessive attitude or attitude rate deviations.

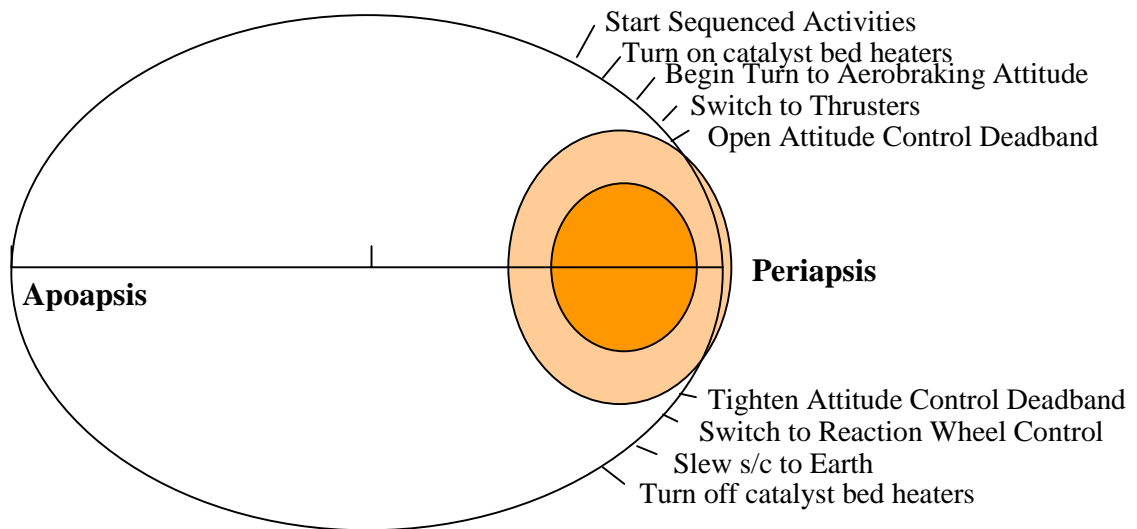


Figure 1. Typical sequence of events for MGS

The sequence is commenced at a specified time before periapsis, which must be known to within approximately a minute. During MGS operations, the time of periapsis was determined by the Navigation team based on Doppler tracking of the spacecraft. If tracking data before and after periapsis are processed, the time of the next periapsis can be determined to within a second. When the resulting satellite orbit is mapped two or more periapses ahead, the prediction error grows rapidly and can become many minutes in a few orbits. This rapid increase in uncertainty is due to the high natural variability of the Martian thermosphere. Occasionally, the MGS team had to update the sequence as many as three times per day.³ The process of evaluating the current orbit, deciding on the need for a maneuver, generating commands, and transmitting and verifying commands is very time consuming. For example, up to 2 hours of tracking data are required after the spacecraft returns to the orbital cruise altitude and communications are established. Another 2 hours may be required to process the data, to verify information, and to send

the maneuver information to the spacecraft. This time allotment does not include round-trip light time, which can be as long as 40 minutes when Mars is at its furthest distance from Earth, about 2.5 AU. This approach requires approximately 4 hours to generate mission critical information about the subsequent orbits. When the orbit period is small, orbit to orbit updating is impractical and the only options are to either accept higher risk or perform less efficient aerobraking. Further complications arise when data drop outs occur. These occurred several times during the MGS mission for as long as two orbits. The intensive workforce required, the increased possibility of human error, and the data drop out problems suggest the search for an autonomous approach to aerobraking using onboard measurements.

Two levels of autonomous aerobraking will be discussed. Level 1 utilizes onboard accelerometers to estimate the change in period due to drag and subsequently to predict the time of periapsis passage of the next orbit so that the aerobraking sequence can be updated. An obvious extension of Level 1 is to have an autonomous periapsis up maneuver performed if some “red line” criterion is exceeded during the aerobraking pass, but this will not be discussed further. Level 2 extends Level 1 to a complete onboard autonomous aerobraking system that would update the aerobraking sequence and implement a maneuver strategy for onboard determination of “up” or “down” propulsive maneuvers. Level 2 would require periodic precision orbit updates. Further enhancement of autonomous operations by including onboard orbit determination capability is of course possible, but would require an additional suite of sensors. Since aerobraking is such a critical operation for mission success, there is no doubt that

frequent tracking passes would be available to receive engineering data. Radio tracking during these passes would automatically provide the necessary data for orbit determination.

1. Level 1 of Autonomous Aerobraking

The feasibility of autonomous aerobraking will depend on the ability to predict the time of periapsis accurately from onboard accelerometers. The time of the next periapsis can be determined once the orbital period is known at the end of the current aerobraking pass. The change in orbital period after a drag pass can be determined several ways. Two methods are evaluated here using Gauss's perturbation equations. In the first, the accelerometer measurement of total change in velocity due to drag is applied as an impulse at periapsis. This method requires minimal onboard processing. For the second method, an integral of the accelerometer data is utilized requiring a limited amount of orbital knowledge and onboard processing. Both methods for determining the change in period were compared with Orbit Propagation Trajectory Generation (OPTG) files that were generated from radio tracking data by the Navigation team during MGS operations. A sample OPTG file is found in Appendix A. The OPTG values of osculating period at apoapsis are taken as the "truth" values and the difference between successive apoapsis osculating periods are taken as the change in period due to drag. No attempts have been made to correct for solar pressure and solar gravity effects on the orbital period. As will be seen later, except during deep orbital resonances (e.g. orbital periods of 1 sol, 1/2 sol, 1/3 sol, etc) the major change in orbital energy from one apoapsis to another is due to drag.

1.1 Method 1-- ΔV Impulse at Periapsis

To estimate the change in period, two body equations will be used starting with Kepler's 3rd Law,

$$(1) \quad P = 2\pi\sqrt{a^3/\mu}$$

where a is the semi-major axis, P is the orbital period and μ is the gravitational constant.

The semi-major axis is a measure of the energy of the orbit and each drag pass reduces the energy by Δa and hence changes the period by

$$(2) \quad \Delta P = \frac{3}{2} \frac{\Delta a}{a} P$$

for the 2-body case. For a higher order gravity field, this is an approximation. Finding the change in semi-major axis will be sufficient for determining the time for aerobraking sequence initiation. The change in semi-major axis is determined by Gauss's perturbation equation⁴,

$$(3) \quad \frac{da}{dt} = \frac{2va^2}{\mu} a_T$$

where v is the velocity and a_T is the tangential acceleration, assumed to be obtained from the accelerometer measurements. The change in semi-major axis can be determined two ways. The first and simplest method is to assume that on the right hand side, semi-major axis and velocity do not change during the aerobraking pass. The integral of Eq. 3 becomes

$$(4) \quad \Delta a = \frac{2v_p a^2}{\mu} \int a_T dt$$

where v_p is the velocity at periapsis. This approach is equivalent to assuming the entire drag pass can be represented by an impulsive maneuver at periapsis. Most precision accelerometers are "integrating" accelerometers, i.e. the acceleration is integrated internally to reduce the noise and the output is the change in velocity over the sample

interval. Data from MGS accelerometers were recorded at 1 Nq as counts representing increments of velocity of 0.332 mm/s. The integral is obtained by simply summing the counts over the aerobraking pass. Of course, accelerometer bias must be removed and is easily calibrated using data taken a few minutes before and after the aerobraking pass. If significant, contributions from angular motion must also be removed.

For the MGS mission, the resulting change in period is estimated, and the comparison with values obtained by radio tracking data is shown in Figure 2. The ordinate is the difference between the estimate using Eq. 4 and the OPTG apoapsis period differences divided by the OPTG values. With a mean of 0.17%, Eq. 4 gives a nearly unbiased estimate of the fractional change in period. The statistics are clearly not homogeneous over the entire mission. For the few orbits before orbit 200 and late in the mission, the maximum acceleration was on average smaller than the rest of the mission. These periods were “walk out” periods where periapsis was continually raised to provide precise orbit control once aerobraking ended. During these orbits and many of the others with large errors, the signal to noise ratio of the accelerometer data decreased resulting in larger relative errors. Nevertheless, over the entire mission, the standard deviation is 7.8% of the actual change in period.

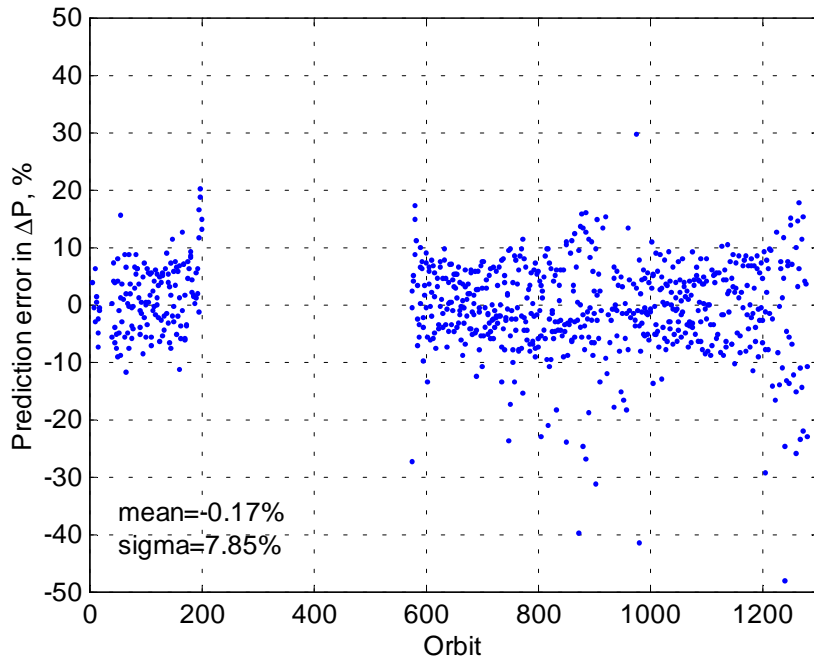


Figure 2. Period change difference between method 1 and radio tracking data.

1.2 Method 2—Complete Integration of Accelerometer Measurements

A second method of approximating the change in period was to integrate the product of acceleration and velocity throughout the drag pass while still assuming a constant semi-major axis. In equation form,

$$(5) \quad \Delta a = \frac{2a^2}{\mu} \int v a_T dt$$

This approach would require additional onboard processing to determine the velocity during the aerobraking pass. Simple two body equations are adequate to estimate velocity. Comparison with the OPTG results is shown in Figure 3. Since velocity only changes a few percent during the aerobraking pass, little difference with Method 1 is noted. However, in both methods, there are some orbits of which a small percent error

still signifies a large time interval. Differences as large as two minutes occurred early in the mission when the orbital period is between 45 hours and 25 hours. These large differences occur during high eccentricity, long period orbits where a small error in estimating the period has a long time to propagate to the next periapsis. Figure 4 shows the difference between Method 2 and OPTG data calculated in seconds. After about orbit 700, the error in period change was within approximately +/- 5 seconds.

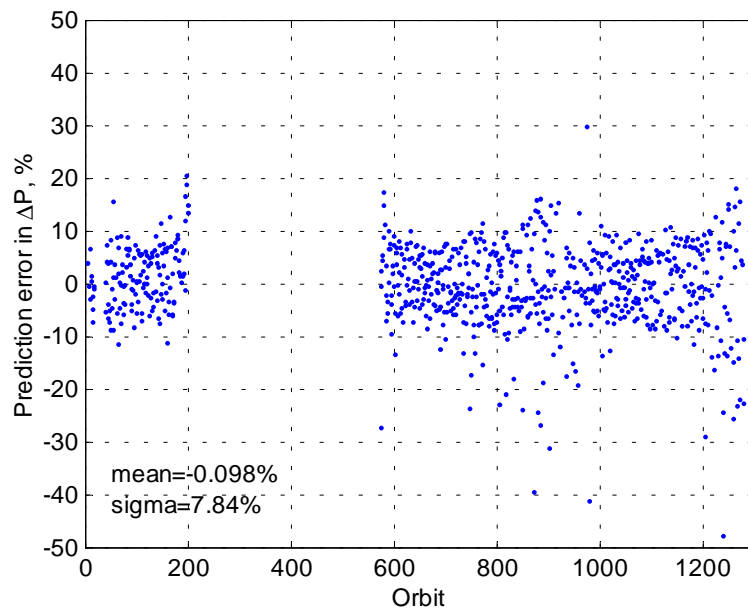


Figure 3. Prediction error in period change between complete integration (method 2) and radio tracking data.

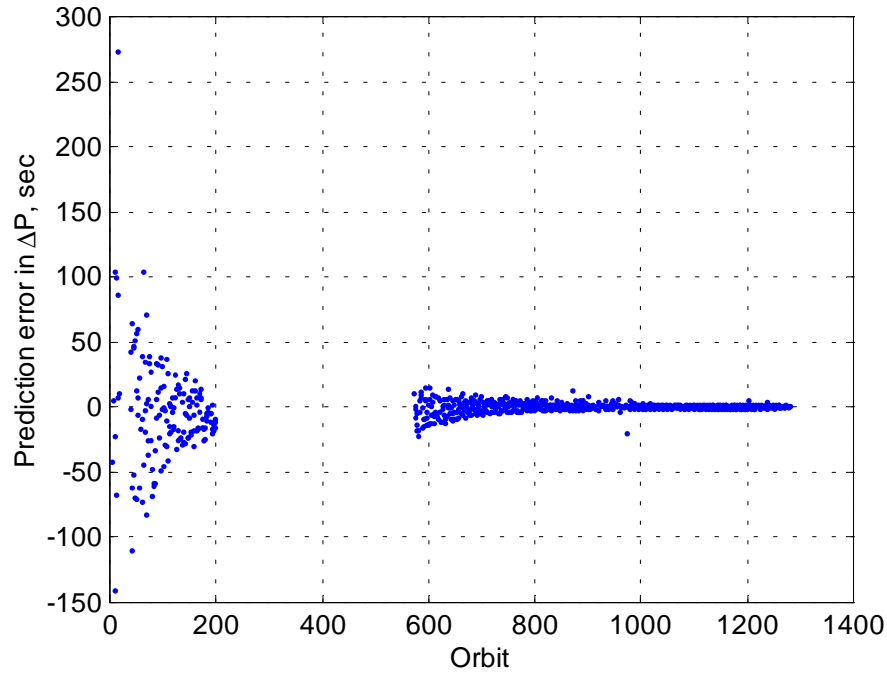


Figure 4. Prediction error in period change between complete integration (method 2) and radio tracking data.

The largest prediction error of approximately 4.5 minutes occurred during orbit 15, a high-density orbit that encountered 150% more drag than any other orbit during the MGS mission. The assumption of a constant semi-major axis will produce an overestimate of the change in period. Further, during this orbit, the s/c performed large attitude excursions and solar array deflections, which may have also contributed to the anomalistic estimate.

1.3 Results of Level 1

To reduce the accumulation of estimation errors after many orbits, a close approximation to the time of periapsis passage can be obtained each pass from the time of maximum

acceleration. For MGS the time of maximum acceleration seldom differed by more than 10 seconds from the time of periapsis. This difference was primarily due to latitudinal gradients in density at a constant geocentric altitude.

By integrating the tangential acceleration data over the aerobraking pass the change in orbital period due to drag can be estimated to less than 8% 1- σ compared to using precise radio tracking methods. Except for orbital periods greater than 24 hours, the time of the next periapsis can be estimated to better than one minute. Once the time of the next periapsis is known, the time to begin the next sequence is determined and preparations can be made to configure the spacecraft for aerobraking or perform a maneuver to raise or lower periapsis. All these calculations can be performed in real time on the spacecraft using only accelerometer measurements, spacecraft orientation, and approximate orbital elements.

2. Level 2 of Autonomous Aerobraking

Level 1 is only a semi-autonomous method of aerobraking since analysis on Earth is still needed to perform the orbit guidance and navigation functions. For full autonomous aerobraking, an accurate trajectory is needed onboard to predict ahead a few orbits to determine what effects the gravity perturbations, solar pressure, solar gravity, and drag will have on subsequent orbits and whether or not a maneuver is needed. For Level 2 simulation, a low order gravity field and atmospheric drag are used for orbit propagation. Solar pressure and gravity may be required in the actual implementation. Inclusion of such terms is straight forward and not considered any further here. It is assumed that the onboard ephemeris will be occasionally updated by the Navigation team, however, no estimates are made herein of the required update frequency.

2.1 Gravity Field

Precision orbit propagation is often necessary to meet science objectives, however during aerobraking, the most important orbital parameter is the periapsis altitude. With atmospheric density scale heights of 5 to 7 kilometers and natural density variability of 25% or more from orbit to orbit⁵, it is only necessary to predict periapsis altitude to between 100 to 200 meters. Carrying any additional accuracy is essentially wasted after the first periapsis passage. For onboard trajectory propagation it is of interest to determine the minimum gravity field that will meet mission requirements.

The spherical harmonic representation of the gravity potential is

$$(6) \quad V(r, \varphi, \lambda) = -\frac{\mu}{r} \left[1 + \sum_{n=2}^{\infty} \left(\frac{R}{r} \right)^n \sum_{m=0}^n (C_{nm} \cos(m\lambda) + S_{nm} \sin(m\lambda)) P_{nm} \sin(\varphi) \right]$$

where λ is longitude, φ is geocentric latitude, and R is a reference radius, usually the mean equatorial radius of the planet. P_{nm} is the associated Legendre polynomial of degree n and order m .⁴ C_{nm} and S_{nm} are spherical harmonic coefficients which are generally determined by tracking satellites of the central body. The most complete Mars gravity field to date is that with $n=75$ and $m=75$, henceforth known as a 75 by 75 or (75,75) gravity field. Each term in the series is called a “solid spherical harmonic” or more simply “spherical harmonic”. The products of P_{nm} and $\cos(m\lambda)$ or $\sin(m\lambda)$ are called “surface spherical harmonics”. Surface spherical harmonics are divided into three classes: zonal harmonics, sectorial harmonics, and tesseral harmonics. Zonal harmonics are those which depend only upon the rotationally symmetric mass distribution about the north-south axis of the planet, so there is no longitudinal dependence and $m=0$. The zonal harmonics are commonly denoted as J terms where $J_n = -C_{n0}$. The effects of J_2 and J_3 ($-C_{20}$ and $-C_{30}$) on orbit evolution are discussed in Section 2.4.

Sectorial harmonics are those in which $n=m$. The sign of these harmonics only depends on longitude; the amplitude varies from pole to pole. Tesseral harmonics are those in which $n \neq m \neq 0$. Tesseral terms change sign with changes in both latitude and longitude and the zero points produce a checkerboard pattern on the sphere.⁶ All non-zonal harmonics have zeros at the poles and in general there are $n-m$ parallels of latitude along which the surface harmonics vanish.

2.2 Validation of Numerical Integration Scheme

A fourth order Runge-Kutta (RK) numerical integration scheme was developed to predict a s/c trajectory several orbits ahead with various size gravity fields. This program was validated against the Program to Optimize Simulated Trajectories (POST) used in flight mechanics analysis. POST is a 6-degree of freedom (6-DOF) trajectory simulation and optimization tool that has been employed in the design and analysis of many planetary exploration missions, including Mars Pathfinder [Tartabini, Paul, private communication]. Aerodynamic, atmospheric and gravitational models can be implemented to simulate trajectories about a planet, providing a history of the translational motion of the spacecraft throughout an aeropass.

Using initial conditions similar to an actual state of a s/c at the beginning of an aeropass mission, POST was used to simulate a 20 by 20 gravity field and predict the trajectory 4 orbits ahead of the initial state. A 20 by 20 gravity field was used for comparison rather than the 75 by 75 gravity field because it takes less time to process. The differences between the 75 by 75 and the 20 by 20 gravity fields are negligible. Using identical initial conditions, a trajectory was predicted 4 orbits ahead using the RK numerical integration. These two trajectories matched periapsis distances to within 0.1 cm after 4 orbits. The time of periapsis passage was within $4e-5$ seconds after 4 orbits. This comparison is shown in Figure 5.

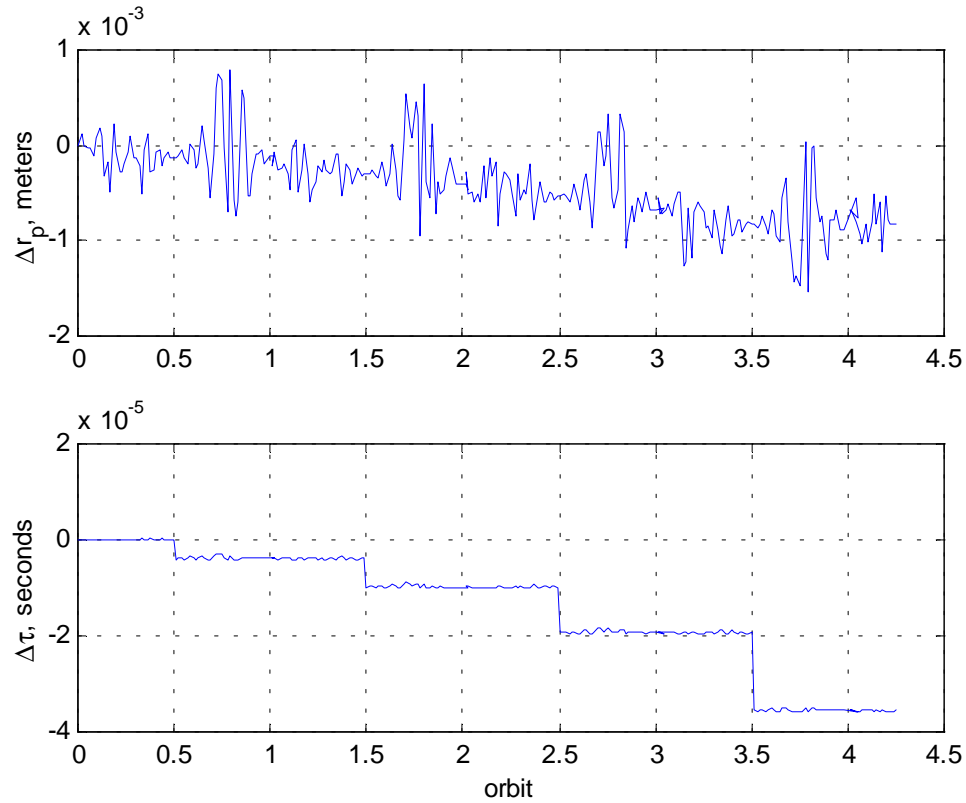


Figure 5. Difference in periapsis distance and time of periapsis between POST 20 by 20 gravity field and RK integration 20 by 20 gravity field

This comparison was done to verify that the numerical integration performed using the RK integration was sufficient to predict orbital mechanics of the s/c after 4 orbits. The POST is a relatively complicated program unnecessary for this analysis. Henceforth, the RK numerical integration scheme is used in this study of autonomous aerobraking.

The following study was done to determine the acceptable number of gravity terms that were needed to predict a trajectory a few orbits ahead to within a 200 meters of the trajectory predicted by a 20 by 20 gravity field.

2.3 Minimum Size Low Order Gravity Field

Once the RK numerical integration scheme was validated for orbital propagation, the number of gravity terms needed to predict a few orbits ahead with accuracy of 100-200 meters was determined. The 20 by 20 gravity field was chosen as the control gravity field by which the smaller gravity fields were compared. Orbital geometry was varied to ensure that the maximum differences between the gravity fields was based on a wide range of periapsis latitudes and longitudes. All integration runs began at apoapsis with a 93° inclination and periapsis distance of 3494.2 km, i.e. periapsis altitude at 100 km. The initial argument of periapsis began at -90° , -45° , 0° , 45° , and 90° and the longitude of ascending node began at 0° , 90° , 180° , and 270° . The initial state was propagated ahead for 9 orbits for 14 different orbital periods to calculate the maximum difference in periapsis distance for each gravity field that was tested. Figures 6, 7, and 8 show a comparison of the (20,20) gravity field with the (3,3), (4,4) and (5,5) gravity fields, respectively. In these figures, P1 indicates the periapsis of the first predicted orbit. P2 indicates the periapsis of the second predicted orbit, etc. The effects of drag and solar pressure are not taken into account in this study.

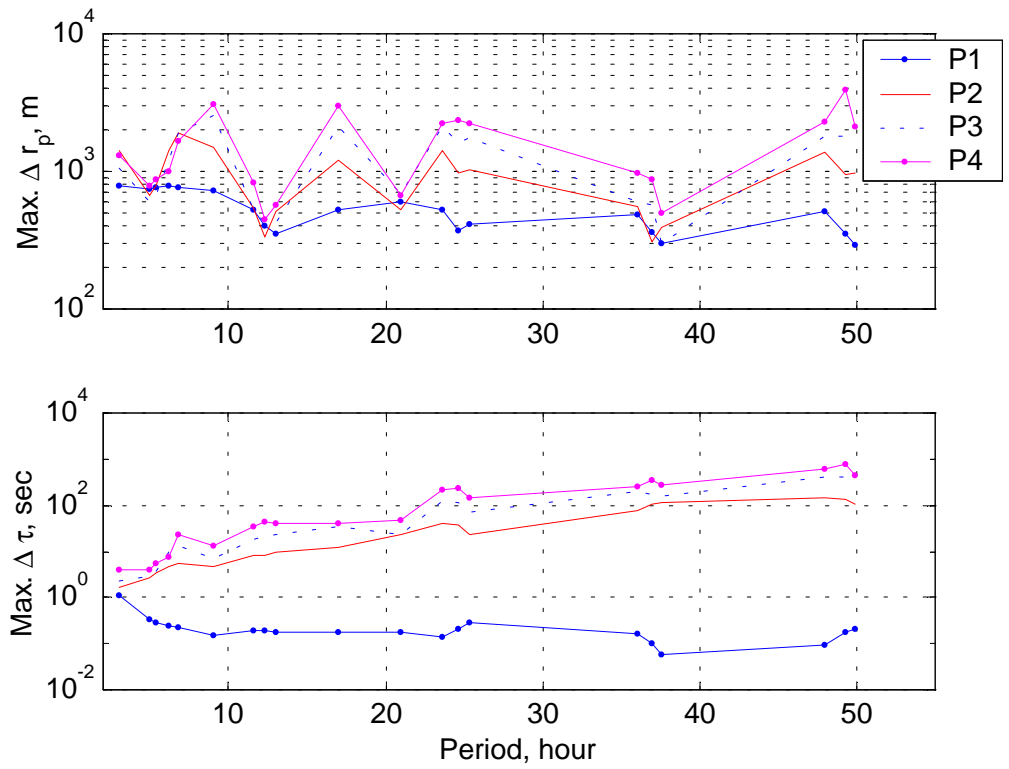


Figure 6. Maximum difference in periapsis distance and time of periapsis passage between a 20 by 20 gravity field and a 3 by 3 gravity field.

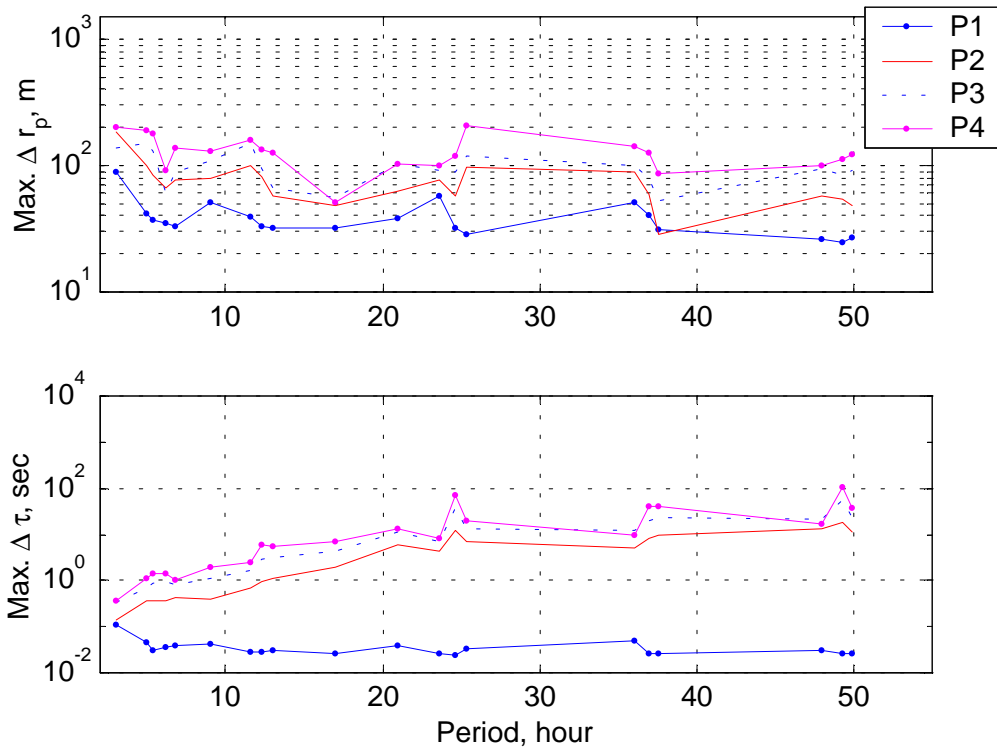


Figure 7. Maximum difference in periastron distance and time of periastron passage between a 20 by 20 gravity field and a 4 by 4 gravity field.

Several peaks are apparent in all of the $\Delta\tau$ and Δr_p plots. These are resonance spikes that appear at 2 sol, 1.5 sol, 1 sol, 1/2 sol, and 1/3 sol, etc., with one sol being approximately 24.6 hours. As seen in Figure 6, the maximum error for the (3,3) field is about 2 kilometers, which exceeds the 100- or 200- meter criterion after 4 orbits. The (4,4) field meets the 200-meter criterion as seen in Figure 6 and the situation is not significantly improved by using the (5,5) field (Figure 8). Except near the resonant periods, the (4,4) field can predict the time of periastron within one minute for 4 orbits. Although different

results may be obtained for specific orbital geometries, it appears that a (4,4) field is adequate for mapping the trajectory for the purpose of onboard maneuver decisions.

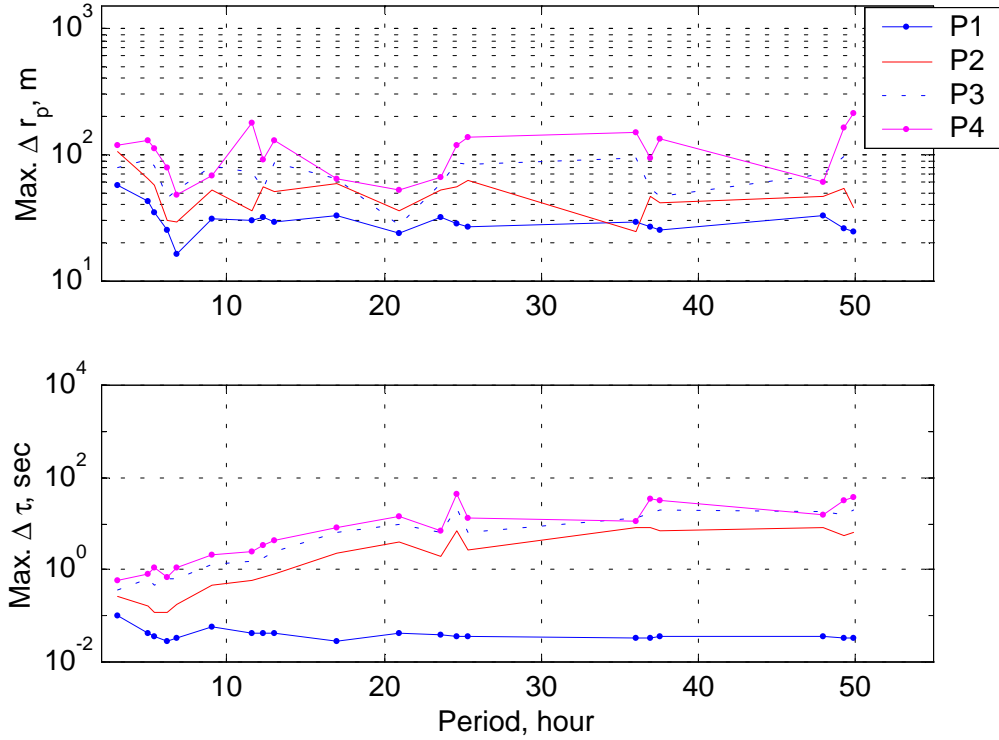


Figure 8. Maximum difference in periapsis distance and time of periapsis passage between a 20 by 20 gravity field and a 5 by 5 gravity field

2.4 Analytic Perturbations

For future interpretation of results it is worthwhile to review the relevant long period and secular perturbations due to the second and third zonal harmonics, J_2 and J_3 . From general perturbation theory⁴, the secular change (linear variation in time) in the longitude of the node and argument of periapsis per orbit due to J_2 are

$$(7) \quad \Delta\Omega = -3\pi J_2 \left(\frac{R}{p}\right)^2 \cos(i)$$

$$(8) \quad \Delta\omega = \frac{3}{2}\pi J_2 \left(\frac{R}{p}\right)^2 (5\cos^2(i) - 1)$$

and the long period changes in eccentricity and inclination due to J_3 are

$$(9) \quad \Delta e = -\frac{3}{4}\pi J_3 \frac{R^3}{ap^2} (5\cos^2(i) - 1)\sin(i)\cos(\omega)$$

$$(10) \quad \Delta i = \frac{3}{4}\pi J_3 \left(\frac{R}{p}\right)^3 (5\cos^2(i) - 1)e\cos(i)\cos(\omega)$$

where $p = a(1 - e^2)$ and for Mars $J_2 = -1.9588e-3$ and $J_3 = -3.1497e-5$. Many missions require nearly sun-synchronous orbits forcing a change in Ω of about 0.53° per day. This can only be accomplished with a high inclination orbit. Other missions may require global mapping capability, again resulting in inclinations near 90° . For such orbits, the argument of periapsis regresses and the latitude of periapsis can change significantly over the aerobraking part of the mission. This is important because of the strong latitudinal gradients in the atmosphere. From Eq. 9 it is also seen that the eccentricity and therefore the periapsis distance will have a long period variation. Atmospheric density is of course most sensitive to periapsis altitude.

2.5 Trajectory Model Implications

The trajectory model described previously was used to simulate 40 orbits with a 4 by 4 gravity field. These results are shown in Figure 9 to illustrate typical changes in the orbital elements. The small change in semi-major axis is due to the small amount of drag for this orbit. The decrease in eccentricity is almost linear. This trend is due to both drag and the J_3 long period perturbations. The trend in inclination is also due to J_3 . The

15 orbit periodic oscillations are primarily due to the third order terms. These cause periapsis to move closer to and further from Mars, depending on the longitude of periapsis. Consequently, if the s/c is approaching a low altitude and the heating at periapsis is approaching the maximum allowable heat limit, it is possible that after a few orbits the gravity terms may raise periapsis. If this were the case, a maneuver could be avoided and ΔV could be saved. Note that the orbit to orbit variation in periapsis altitude can be about 1 kilometer, so that up to 20% orbit to orbit density variations might be expected due to gravity perturbations alone.

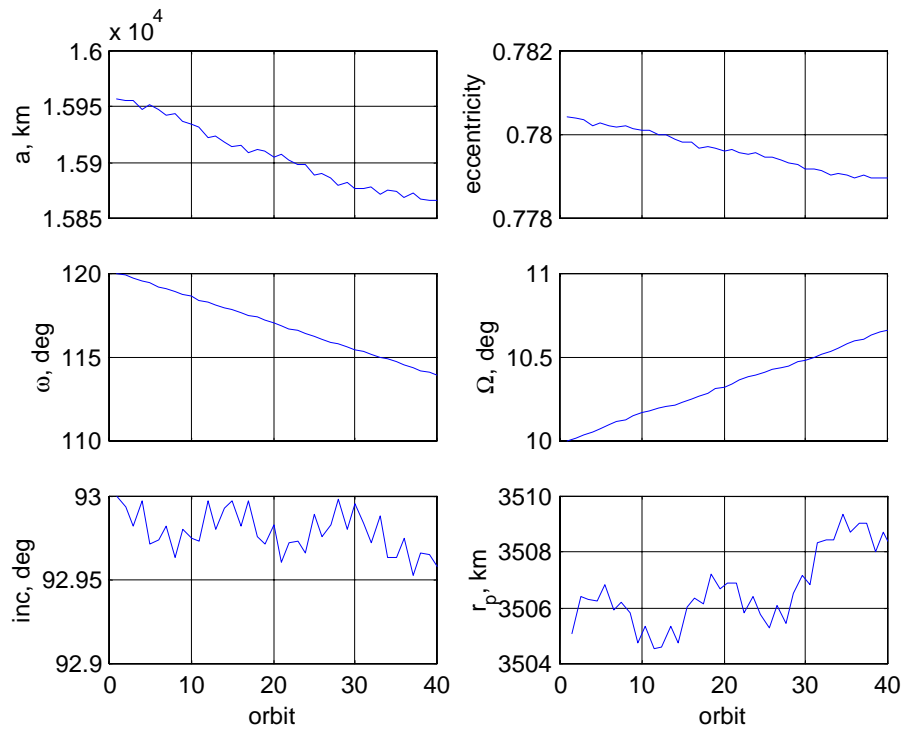


Figure 9. Forty orbits integrated with a 4 by 4 gravity field and drag.

2.6 Atmospheric Model

For fully autonomous aerobraking, the onboard measurements of acceleration during the drag pass will be used directly in the equations of motion. This approach was validated during the Level 1 discussion. Consequently, no global atmospheric model will be necessary. However, to predict drag for subsequent orbits, some sort of model is required for maneuver decision purposes. The process for developing this model is not simulated in this study, but is reasonably well understood because it is simply an onboard implementation of the ground based process used for MGS². In this process, accelerometer data are converted to atmospheric density (ρ) and a least square fit to $\log(\rho)$ versus altitude provides density at periapsis and local scale height. These two parameters are then used to predict density for subsequent orbits. In addition, a sliding least square fit using these density and scale height values would be used to determine any wave structure in the atmosphere⁷. In the simulations presented later, a simple atmospheric model with linear scale heights over specified altitude ranges is used with the wave model and statistics from reference 7. These statistics account for all of the processes discussed above. Hence, in the simulations, density is modeled as

$$(11) \quad \rho(h, \phi, \lambda) = \rho_o(h, \phi) \left[A_o + S(t) + \sum_1^3 A_n \sin(n(\lambda - \lambda_n)) \right]$$

where ρ_o is a function of altitude and latitude from the linear scale height model. A_o is a random variable with mean 1 and standard deviation between 0.15 and 0.19⁷. The randomness in A_o accounts for unmodeled variations in the atmosphere and errors due to the density and scale height estimation process. S is included to simulate a dust storm. Figures 10 and 11 illustrate the variation of density (ρ_o) and scale height with altitude and

latitude from a thermospheric model. For example, Figure 10 is a plot of density vs. altitude for latitudes of 0° to 90° in 15-degree increments. The $+90^\circ$ line is closest to the text representing that latitude value. This model is only valid around $L_s = 270^\circ$, i.e. northern hemisphere winter. In the same manner, Figure 11 is a plot of scale height vs. altitude for the same range of latitudes.

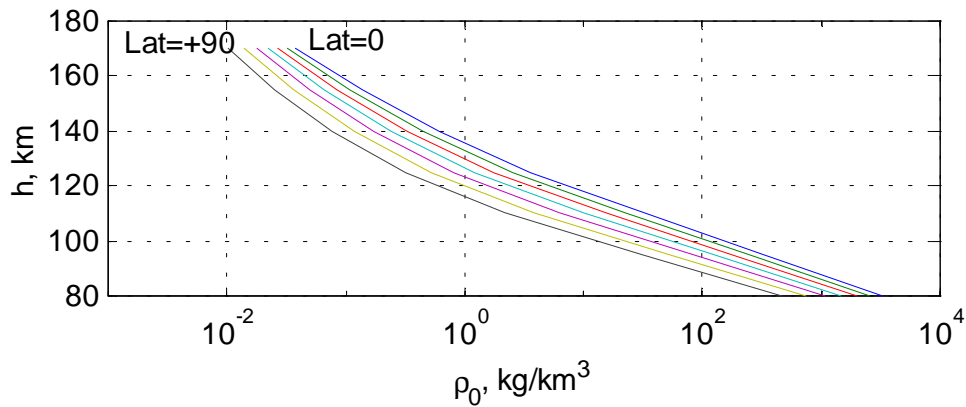


Figure 10. Density in northern hemisphere from thermosphere model

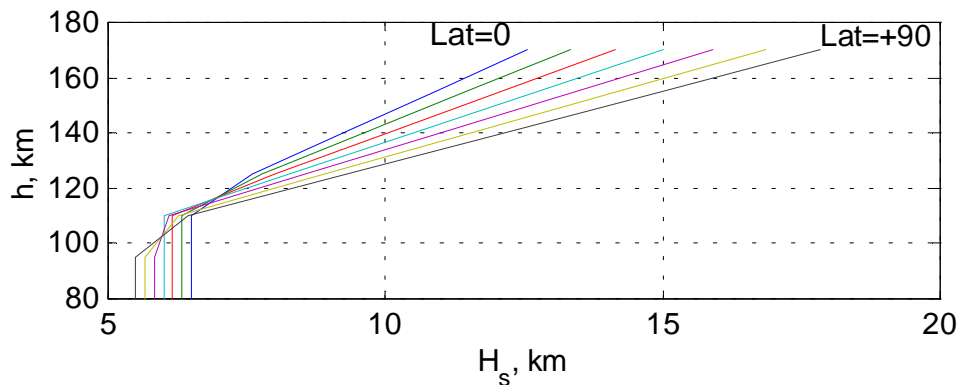


Figure 11. Scale height in northern hemisphere from thermosphere model

During MGS a regional dust storm caused density to increase by more than a factor of two in a few orbits. Any onboard autonomous algorithm will have to account for such

storms. The specific time dependence assumed for S will be discussed later. The remaining term represents three stationary waves. Amplitude and phases are given in Appendix B and except for the storm term, the model is the same as that given in reference 7.

2.7 Maneuver Strategy

Spacecraft that are performing aerobraking will have thermal, structural or other constraints that require aerobraking to be performed within certain limits. For Magellan, MGS, Mars Climate Orbiter, and Odyssey, the constraint was the maximum temperature of the solar arrays. In general, this means that aerobraking has to take place below a maximum allowable free stream heat flux. Aerobraking must also take place above a lower limit to complete the aerobraking phase in a reasonable or designed time. The region between these two limits is termed the “corridor”. The upper limit of this corridor is a function of the orbit geometry because the duration of an aerobraking pass and the velocity during the pass change as the orbit becomes more circular. The corridor is generally specified in terms of free stream heat flux because this is a meaningful surrogate for both the temperature reached by the structure and the efficiency of aerobraking.

Selecting a maneuver strategy to stay within a specified corridor requires a knowledge of the phenomena that are causing the orbit to move out of the corridor. Typically it is advantageous to minimize the maneuver propulsive requirements, minimize the number of maneuvers, and maximize the time between maneuvers for ground operations work

load. For autonomous aerobraking only the first two considerations are important. For the purposes here, a rather simple strategy is utilized to demonstrate feasibility.

The maneuver corridor is illustrated in Figure 12. The corridor is defined in terms of heat flux, Q , vs. apoapsis altitude. Since periapsis altitude is constant within a few 10's of kilometers, period, semi-major axis or periapsis velocity would have been equally valid independent variables. When apoapsis is high, the duration of aerobraking is short compared to the characteristic time for conduction to transfer the aerodynamic heating to sensitive areas of the spacecraft. In this region, aerobraking is over before maximum temperature is reached on some s/c components. As the orbit becomes less eccentric, aerobraking duration increases and the maximum Q must be lower. Late in the mission, when apoapsis altitude is below about 1000 km, the lifetime of the orbit may become the limiting factor. To assure a minimum lifetime in case communications are lost may require much lower drag. This is illustrated by the steep slope between 1000 and 400 kilometers. For this simple case, the lower boundary is set at $\frac{1}{2}$ of the upper boundary. The red line at the top of the figure is the "immediate up maneuver boundary." If during a pass, the maximum Q exceeds this limit, a maneuver is performed at the next apoapsis to raise periapsis a pre-specified distance. For example, one density scale height might be used if the violation is "small" and 2 scale heights for gross violations. Selecting the relative locations of these three boundaries is an essential step in assuring successful, safe, and efficient aerobraking. The corridor boundaries are usually determined through a process of manually varying the limits, performing mission simulations, and observing the feasibility and efficiency of the aerobraking phase.

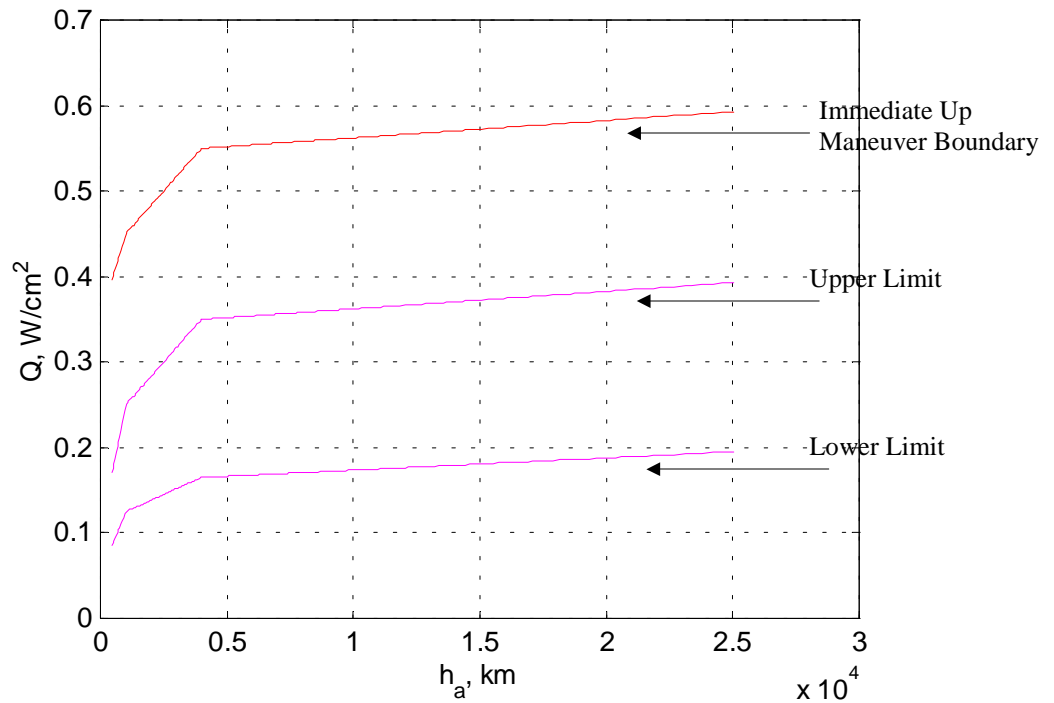


Figure 12. Maneuver corridor.

Coupled with the definition of the corridor is the issue of what criteria to use after each aerobraking pass to decide if a maneuver is necessary. Simply using the maximum Q for each pass leads to either excessive maneuvers or inefficient aerobraking because of the large natural variability of the Martian thermosphere. During the MGS aerobraking mission, when very little was known about the variable nature of the thermosphere, the five orbit running mean was utilized to make maneuver decisions. If two successive five orbit means fell outside the corridor, a maneuver was performed. The decision was sometimes preempted by human judgment based on wave model predictions or other considerations.

For the simulations, maneuver decisions are made at each apoapsis. The decision is based on predicting three periapses ahead using only the deterministic components of the atmospheric model described by Eq. 11. If the average heat flux from these predicted orbits is outside of the corridor, a maneuver is performed to target the average Q to the middle of the corridor. A tangential ΔV is applied at the current apoapsis, changing the osculating semi-major axis and eccentricity. The orbit is then propagated to the next apoapsis where the process is repeated. During this propagation, the random components of Eq. 11 are included. Aerobraking ends when the apoapsis altitude becomes 400 km, the assumed altitude for the circular science orbit. Not included in this simulation is consideration of other desired terminal conditions on the science orbit, e.g. nodal regression or conditions for a frozen orbit.

2.8 Typical Mission Simulation

Figures 13 and 14 show results from a typical simulation of a mission without a dust storm. Figure 13 provides information of interest to the maneuver strategy while Figure 14 shows orbit parameter evolution over the mission. The initial orbit is approximately the same as the expected Mars Odyssey initial orbit. Referring to Figure 13, the heat flux corridors are shown for each orbit. The initial periapsis is about 20 km above the first aerobraking orbit. During the first several orbits the periapsis altitude is gradually decreasing to allow the *s/c* to ‘walk-in’ to the atmosphere. For this simulation, the maximum decrease in periapsis altitude is 5 km per maneuver and 2 orbits are spent at each altitude. Maximum density follows maximum Q on an orbit to orbit basis with a gradual change in the ratio as the orbit becomes less eccentric and periapsis velocity

decreases. Until orbit 150, the latitude of periapsis is increasing and both the J_3 term and the shape of the reference ellipsoid contribute to increasing the areodetic altitude from orbit to orbit. Thus, maneuvers during the first 150 orbits tend to be “down” maneuvers, continually decreasing areodetic altitude, h . There is one “up” maneuver near orbit 60 due to an unusually high density. After orbit 150 these two factors tend to decrease periapsis areodetic altitude with the second “up” maneuver near orbit 175. The total ΔV required for the mission is 3.9 m/s. In the plot, a positive (negative) ΔV means periapsis is raised (lowered). Near the end of the mission, the maneuvers raise periapsis as the corridor shifts to much lower values of Q due to both heating and lifetime constraints. The aerobraking mission is completed in about 61 days after 241 orbits and the period has been reduced from 17 hours to 1.9 hours. Only 10 orbits exceeded the upper limit of the corridor and none exceeded the immediate up maneuver boundary.

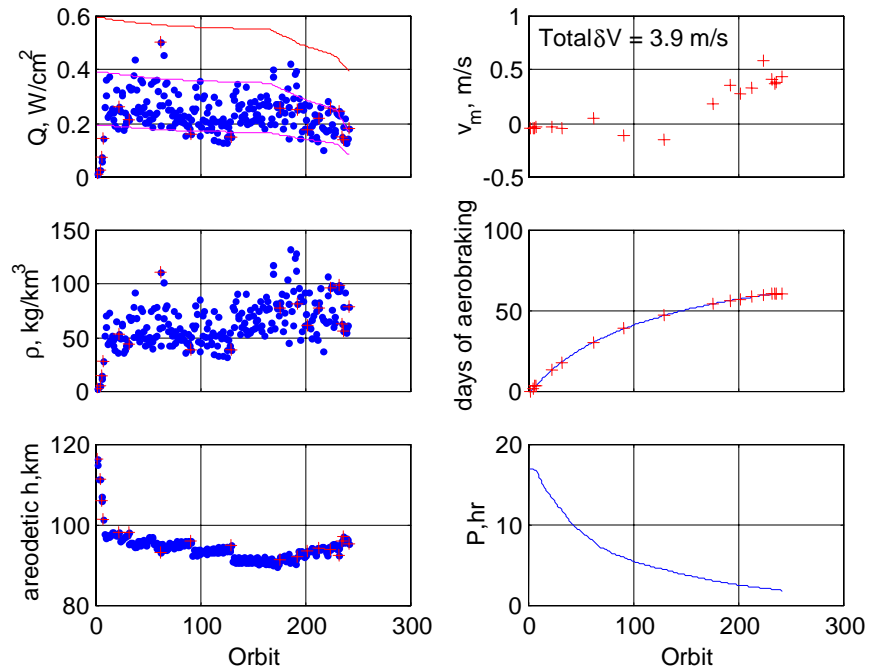


Figure 13. Maneuver related parameters for a typical maneuver strategy.

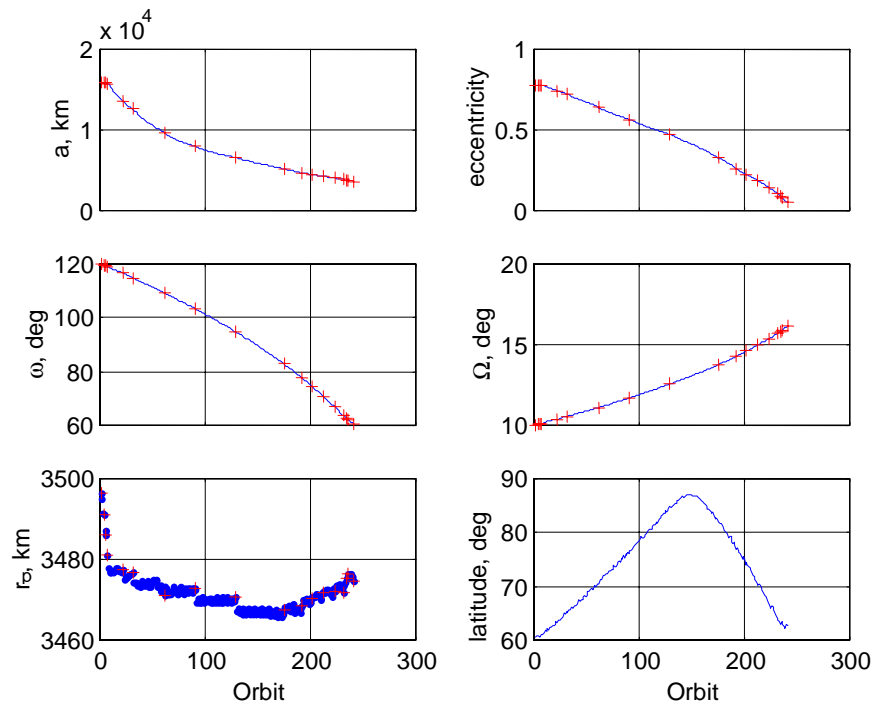


Figure 14. Orbit parameter evolution for a typical maneuver strategy.

2.9 Effects of Corridor Variation

The previous section detailed results of a typical maneuver strategy on an aerobraking mission. This section will discuss the effects of varying the corridor on the time of aerobraking and the amount of ΔV used in aerobraking.

For the typical mission simulation, maneuver strategy 1, the maneuver as a function of apoapsis altitude is shown in Figure 15.

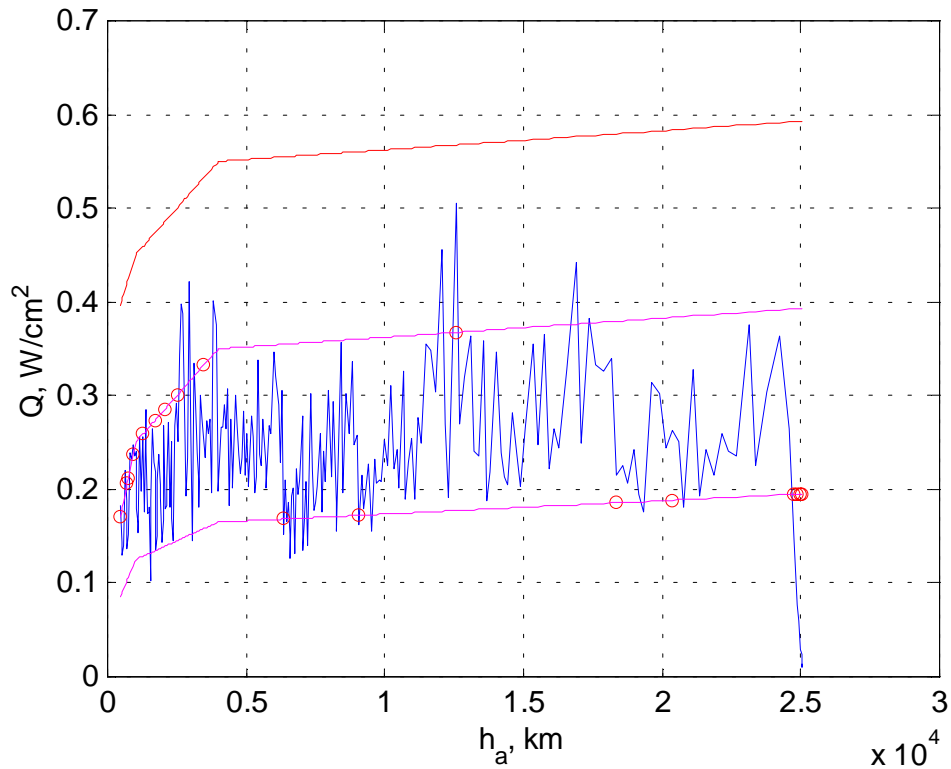


Figure 15. Maneuver strategy 1 .

As shown, there are no violations of the “immediate up maneuver” boundary, and as discussed in the previous section, aerobraking was completed in 60 days utilizing 18 maneuvers for a total ΔV of 3.9 m/s.

Lowering the maneuver corridor will reduce the risk of overheating the s/c, but will significantly lengthen the duration of aerobraking and may increase the amount of ΔV used for the mission. Figure 16 shows maneuver strategy 2, a mission that utilizes a lower and narrower maneuver corridor. The duration of aerobraking is increased to 110 days, and 42 maneuvers use a total ΔV of 11.1 m/s.

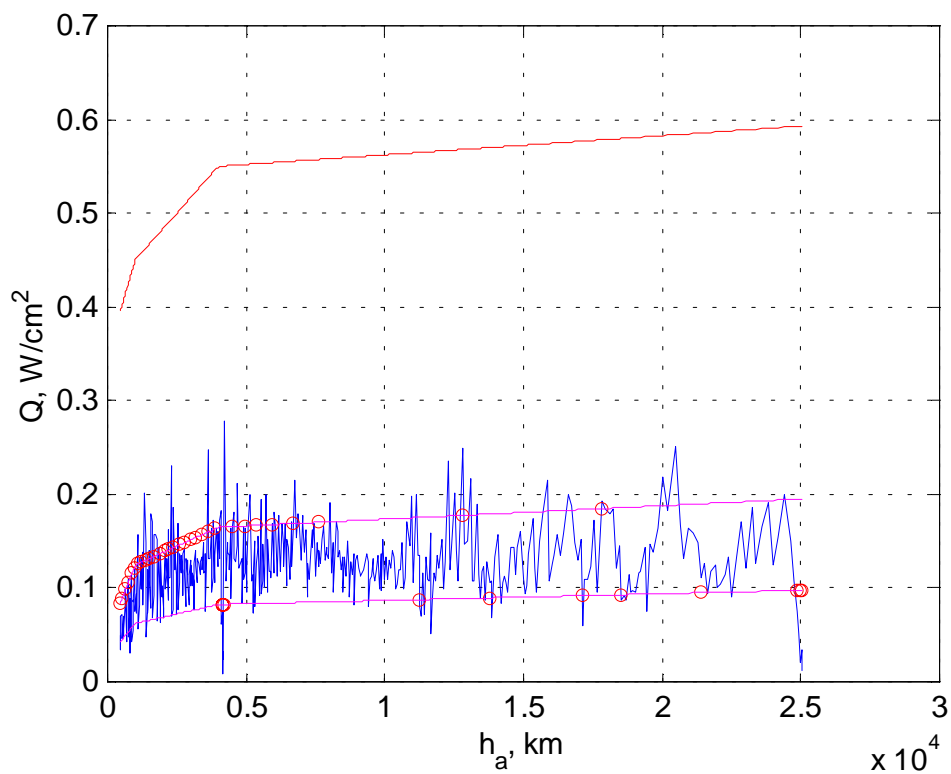


Figure 16. Maneuver strategy 2.

A maneuver corridor that is larger and that allows a higher heat rate will of course increase the risk of overheating the s/c but may reduce the number of aerobraking maneuvers. Figure 17, maneuver strategy 3, is a larger corridor raised close to the heating limits of the s/c.

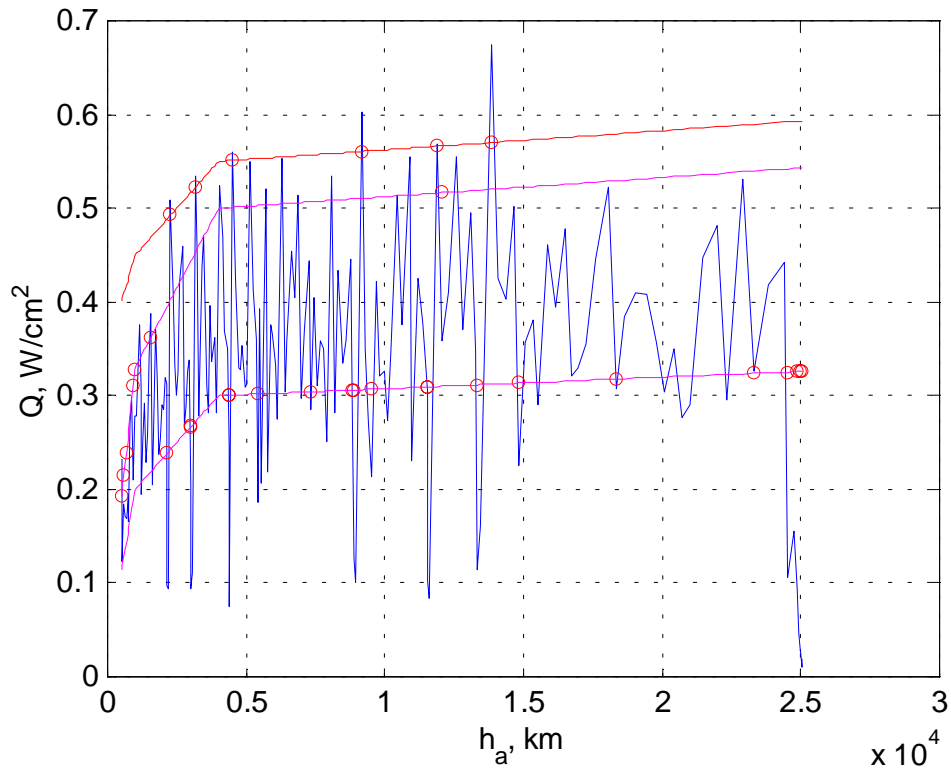


Figure 17. Maneuver strategy 3.

As shown, there are six violations of the immediate up maneuver boundary, causing the s/c to immediately raise periapsis and slowly walk back into the atmosphere. The s/c, therefore, alternates between up and down maneuvers, flying deep into and out of the atmosphere, generating inefficient aerobraking. There were 33 maneuvers made producing a total ΔV of 8 m/s.

Figure 18 shows maneuver strategy 4. This strategy is similar to maneuver strategy 3, but the corridor is narrower. The upper heat flux limit is lowered while the lower heat flux limit is the same as in maneuver strategy 3. The s/c does not violate the immediate up maneuver boundary, and it completes aerobraking in 45 days, utilizing 32 maneuvers for a total ΔV of 3.55 m/s.

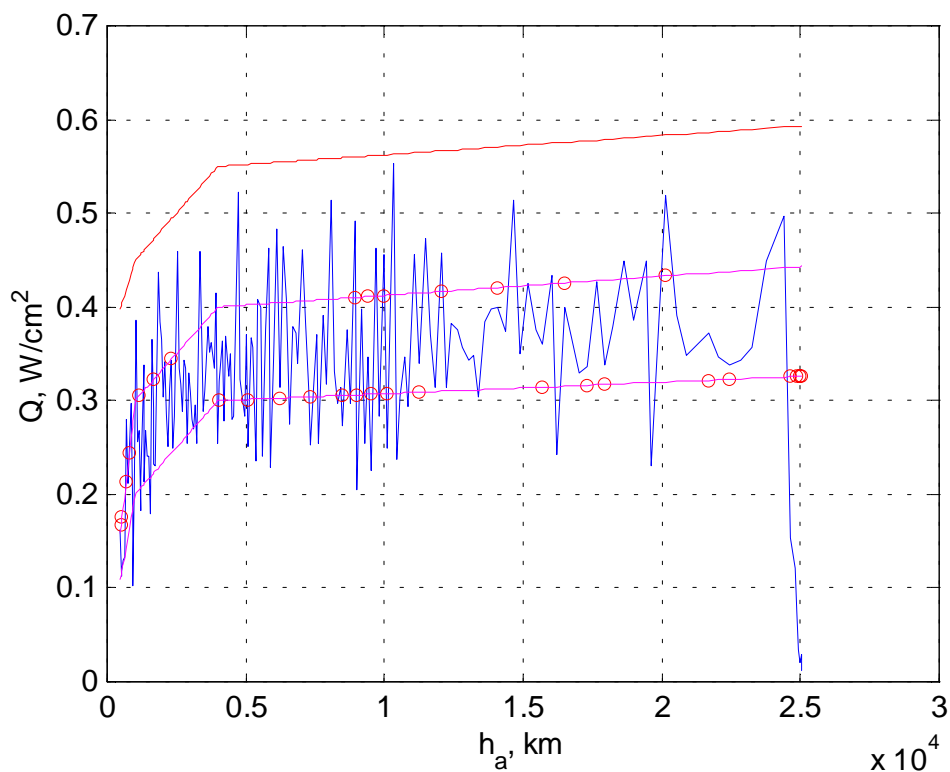


Figure 18. Maneuver strategy 4.

2.10 Dust Storm Mission Simulation

Dust storms are common occurrences on Mars during southern hemisphere summer. Storms can be limited to small areas of the planet or can be global in nature. The storm encountered during MGS was a regional storm in the southern hemisphere but influenced the thermosphere in the northern hemisphere in a matter of days. When a dust storm occurs, the dust absorbs some of the solar energy that would normally reach the surface of the planet. The energy is transferred to the atmosphere, which expands as it is heated. Local expansion is usually balanced by subsidence at other locations. Hence complex dynamics are triggered in the atmosphere that can cause significant variations in density

on a global scale. Except for the MGS data, little is known about the characteristic of thermospheric density variations during a storm. It is thought that the atmosphere responds in a few days and then decays over time scales of a month. To simulate such a dust storm it is assumed that the storm starts on the 20th day of aerobraking and increases the nominal density by a factor of 2.6, i.e. $S=1.6$ in Eq. 11. The density shift then decreases exponentially with a decay time of 25 days,

$$(12) \quad S(t) = 1.6e^{-\frac{(d-20)}{25}}$$

where $d > 20$ is the number of days since aerobraking began.

Results of this simulation are shown in Figure 19 and are to be compared with Figure 13 for the case without a storm. The first periapsis after day 20 had $Q=0.95$ and is plotted as a “+” at the top of the figure. Density jumped from values near 70 to 190. Since this exceeded the “immediate up maneuver boundary,” a maneuver was performed to raise periapsis to about 110 km. Walk-in begins on the next orbit with a 5 km decrease in altitude and, after the second maneuver, Q is back in the corridor. In practice, the walk-in might be delayed to permit additional time to evaluate the situation. The periapsis altitude remains higher than the typical mission because of the storm and does not return to the altitudes of the typical mission without the storm (Figure 13) until around orbit 200. After the storm, Q on average is lower than the typical case values because an extra margin of safety is automatically included in the post-storm strategy. The time to complete aerobraking takes an extra 14 orbits and 4 days but only 0.1 m/s extra ΔV .

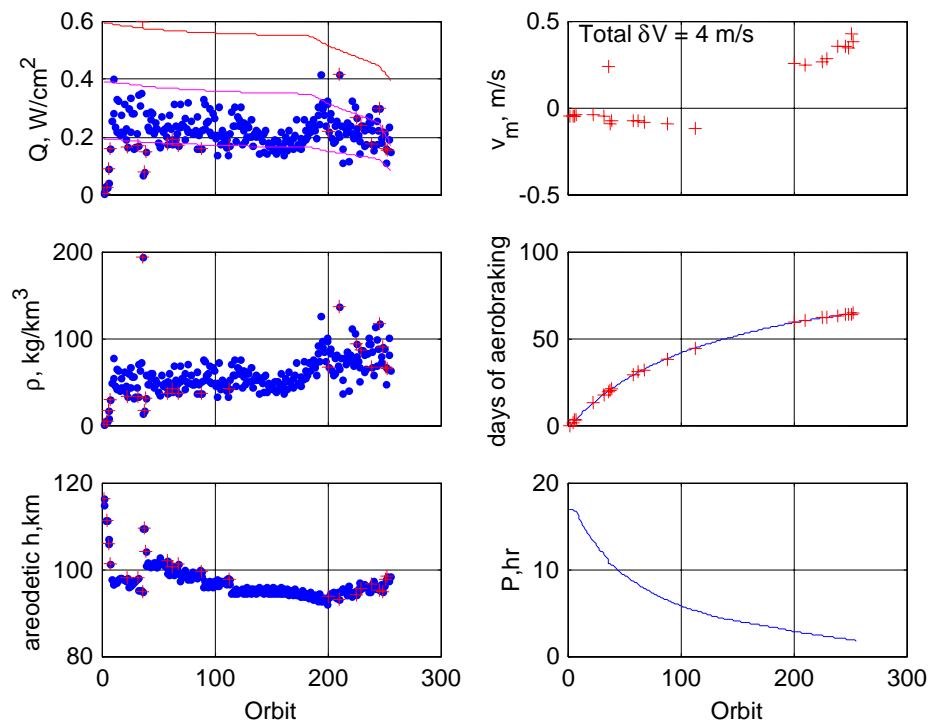


Figure 19. Maneuver parameters for the dust storm case.

Concluding Remarks

Autonomous aerobraking at Mars would significantly reduce the intensive workforce required during aerobraking operations and would reduce the potential for human error. Two levels of autonomous aerobraking have been presented. The simple Level 1 approach would predict the time for initiating the aerobraking sequence and can be implemented with simple algorithms without significant impact on most Mars orbiters. An approach for a completely autonomous system, level 2, has been presented at the feasibility level. Further development should focus on a particular mission and spacecraft to provide the next level of detail, develop maneuver strategies consistent with mission and s/c constraints, and validate and integrate data processing algorithms.

The focus of this thesis was the feasibility of utilizing a simple model for autonomous aerobraking. Orbital and heating considerations were addressed as primary drivers for a maneuver strategy. There are numerous additional issues that should be considered. Each aerobraking mission will have particular end of aerobraking conditions that must be considered, however, they were not addressed in this thesis because they are mission dependent. A complete Level 2 autonomous system must also consider s/c subsystem performance during each orbit. For example, by maintaining an onboard ephemeris, spacecraft orientation with respect to the Sun and Earth would be known and used for solar array and antenna pointing, respectively. Also, temperature measurements at critical points would be correlated with measured drag acceleration parameters to automatically adjust corridor boundaries based on the real limitations rather than surrogate variables. Spacecraft maintenance operations, such as star tracking for

quaternion updates, will have to be included in designing the autonomous sequence. Error detection and safing strategies must also be included. Future work in the area of autonomous aerobraking includes testing these approaches with actual flight data. Currently, level 1 is scheduled to be tested during aerobraking operations of Mars 2001 Odyssey. Also, hardware must be built to test the feasibility of onboard processing.

Finally, maneuver results are not comparable with Mars 2001 Odyssey project simulations for a variety of reasons. Quite properly, the project is using a more conservative error model for both the atmospheric model and the corridor and the Odyssey maneuver strategy must include operational constraints that are unnecessary for autonomous operations.

A portion of this thesis was written for publication for the AAS/AIAA Astrodynamics Specialist Conference in Quebec City, Canada⁸.

References

- ¹ Lyons, D.T. “Aerobraking Magellan: Plan versus Reality”. AAS/AIAA Spaceflight Mechanics Meeting, Cocoa Beach, Florida, February 14-16, 1994. Paper AAS 94-118
- ² Tolson, R.H., Keating, G.M., Cancro, G.J., Parker, J.S., Noll, S.N., and Wilkerson, B.L. “Application of Accelerometer Data to Mars Global Surveyor Aerobraking Operations”. *Journal of Spacecraft and Rockets*. Vol. 36, No. 3, May-June, 1999. pp. 323-329.
- ³ Lyons, D.T. “Aerobraking Automation Options”. AAS/AIAA Astrodynamics Specialist Conference, Quebec City, Canada. July 30-August 2, 2001. AAS 01-385.
- ⁴ Battin, R.H., **An Introduction to the Mathematics and Methods of Astronautics**. AIAA Education Series, 1987.
- ⁵ Tolson, R.H., Keating, G.M., Noll, S.N., Baird, D.T., Shellenberg, T.J. “Utilization of Mars Global Surveyor Accelerometer Data for Atmospheric Modeling”. AAS/AIAA Astrodynamics Specialist Conference, Girdwood, Alaska. August 16-19, 1999. AAS 99-206.
- ⁶ Chobotov, V.A. **Orbital Mechanics**. AIAA Educational Series, Washington, 1991.
- ⁷ Dwyer, A.M., Tolson, R.H., Munk, M.M., Tartabini, P.V. “Development of a Monte Carlo MarsGRAM Model for Mars 2001 Aerobraking Simulations”. AAS/AIAA Astrodynamics Specialist Conference, Quebec City, Canada. July 30-August 2, 2001. AAS 01-389
- ⁸ Hanna, J.L., Tolson, R.H., “Approaches to Autonomous Aerobraking at Mars”. AAS/AIAA Astrodynamics Specialist Conference, Quebec City, Canada. July 30-August 2, 2001. AAS 01-387.

Appendix A. Sample OPTG File

CCSD3ZS00001AAAAAAAAANJPL3KS0L015BBBBBBBB

MISSION_NAME = MARS_GLOBAL_SURVEYOR;

SPACECRAFT_NAME = MARS_GLOBAL_SURVEYOR;

DATA_SET_ID = OPTG;

FILE_NAME = optg_i_971005_OD015_021_V2;

PRODUCER_ID = NAV;

APPLICABLE_START_TIME = 1997-278T13:40:00.000;

APPLICABLE_STOP_TIME = 1997-289T12:00:00.000;

PRODUCT_CREATION_TIME = 1997-280T09:44:50;

CCSD3RE00000BBBBBBBNJPL3IS00357CCCCCCCC

\$\$MGS ORBIT PROPAGATION AND TIMING GEOMETRY FILE v001

* OPTG optg_i_971005_OD015_021_V2.txt

* TITLE MGS Aerobraking GIN Lock File: OPTG File

* CREATION JPL 97-OCT-07/09:44:50

* BEGIN SCE 97-OCT-05/13:40:00.000

* CUTOFF SCE 97-OCT-16/12:00:00.000

* PFILE JPL 97-OCT-07/09:42:21

* PVDRIVE JPL 97-JUN-04/14:45:25

* TWIST JPL 97-JUN-03/18:10:26

* ORBIT INSERTION

* ORBIT BOUNDARY PERIAP 14

\$\$EOH

CONST, MARS, 1997-278T13:40:00.000, 2.450727069444444E+06, 63.182, 14,
+00000T01:26:25.647, 5.232351691705257E+01,
0.0,

3.176810000000000E+02, -1.080000000000000E-01,
5.288600000000000E+01, -6.100000000000000E-02,
1.768680000000000E+02, 3.508919830000000E+02,
3.393400000000000E+03, 3.393400000000000E+03, 3.493400000000000E+03,
5.208300000000000E-03,

APOAP, MARS, 1997-279T07:13:28.716, 2.450727801026800E+06, 63.182, 14,
-00000T18:59:55.056, 5.212633532759161E+01,

2.727891366691909E+04, 8.718465123090429E-01, -1.799999999999999E+02,
1.203582824387599E+02, 3.592193333595955E+02, 1.198628996713515E+02,
9.331350377583626E+01, 3.196854532660352E+02, 1.467615311919486E+02,
2.716993494777135E+08, 4.767382450585361E+04,

LDTERM, MARS, 1997-279T07:43:35.797, 2.450727821942095E+06, 63.182, 14,
-00000T18:29:47.905, 5.212063988388455E+01,

AEQUAX, MARS, 1997-279T22:44:40.706, 2.450728447693361E+06, 63.182, 14,
-00000T03:28:41.885, 5.194684373163146E+01,

1.044752504323481E+02,

NPOLEX, MARS, 1997-280T02:01:11.711, 2.450728584163318E+06, 63.182, 14,
-00000T00:12:11.678, 5.190534290316390E+01,

9.542138473202795E+02,
 EOCCAB, MARS , 1997-280T02:10:14.892, 2.450728590450136E+06, 63.182, 14,
 -00000T00:03:06.486, 5.190313695887239E+01,
 2.380455547883421E+02, 4.773902464491786E+01,
 EOCCSB, MARS , 1997-280T02:12:27.716, 2.450728591987449E+06, 63.182, 14,
 -00000T00:00:53.452, 5.190259963491549E+01,
 2.363999702607257E+02, 3.749859447214319E+01,
 DLTERM, MARS , 1997-280T02:13:16.164, 2.450728592548199E+06, 63.182, 14,
 -00000T00:00:05.045, 5.190240472586776E+01,
 PERIAP, MARS , 1997-280T02:13:21.213, 2.450728592606636E+06, 63.182, 15,
 +00000T00:00:00.000, 5.190238445549247E+01,
 2.704935857476463E+04[†], 8.706788971378293E-01, 2.153498505310610E-10,
 1.203592202924661E+02, 3.592379947334120E+02, 1.197286446768719E+02,
 9.330705436660348E+01, 3.197002649401871E+02, 1.466186994455514E+02,
 2.722364288771998E+08, 1.100134528364190E+02,
 8.942137036421834E+01, 1.689273689322780E+02,
 9.033861349904177E-01, 7.827125649582756E-08,
 3.305901828706264E+02, 4.340342248274596E-01,
 1.100000000000000E+02, 7.843341969754264E-08,
 EOCCSE, MARS , 1997-280T02:19:05.584, 2.450728596592402E+06, 63.182, 15,
 +00000T00:05:43.419, 5.190102571855694E+01,
 2.326658518568022E+02, 7.248925572352138,
 DEQUAX, MARS , 1997-280T02:20:50.772, 2.450728597809866E+06, 63.182, 15,
 +00000T00:07:28.352, 5.190062174559076E+01,
 2.318183823292407E+02, 16:55:32,
 EOCCAE, MARS , 1997-280T02:21:09.946, 2.450728598031783E+06, 63.182, 15,
 +00000T00:07:47.494, 5.190054871375866E+01,
 2.316672088181590E+02, -1.271479188782414,
 SPOLEX, MARS , 1997-280T02:37:14.973, 2.450728609201071E+06, 63.182, 15,
 +00000T00:23:53.487, 5.189707995503292E+01,
 3.973764929465043E+03,
 LDTERM, MARS , 1997-280T19:20:28.013, 2.450729305879779E+06, 63.182, 15,
 +00000T17:07:06.133, 5.171013166651568E+01,
 APOAP, MARS , 1997-280T20:26:21.034, 2.450729351632340E+06, 63.182, 15,
 -00000T18:12:59.349, 5.169776280329449E+01,
 2.652499642199344E+04, 8.682058085831267E-01, -1.79999999999952E+02,
 1.203482709777643E+02, 3.592498322428532E+02, 1.197567785682977E+02,
 9.329266733114435E+01, 3.197044325673348E+02, 1.466410909815206E+02,
 2.727198284058618E+08, 4.616607174431264E+04,
 AEQUAX, MARS , 1997-281T11:14:10.371, 2.450729968175587E+06, 63.182, 15,
 -00000T03:25:28.733, 5.152756461938302E+01,
 2.909691772379048E+02,
 NPOLEX, MARS , 1997-281T14:27:26.693, 2.450730102392283E+06, 63.182, 15,
 -00000T00:12:13.147, 5.148691365644056E+01,
 9.604673261513244E+02,
 EOCCAB, MARS , 1997-281T14:36:46.555, 2.450730108872170E+06, 63.182, 15,
 -00000T00:02:51.321, 5.148464844394982E+01,
 6.510256215592129E+01, 4.663033943940896E+01,
 DLTERM, MARS , 1997-281T14:39:05.488, 2.450730110480189E+06, 63.182, 15,
 -00000T00:00:32.199, 5.148408913087167E+01,
 EOCCSB, MARS , 1997-281T14:39:18.121, 2.450730110626396E+06, 63.182, 15,
 -00000T00:00:19.570, 5.148403851767003E+01,
 6.330070513914555E+01, 3.495941477970037E+01,

[†] semi-major axis of MGS for orbit 15.

Appendix B. Atmospheric Wave Model⁷

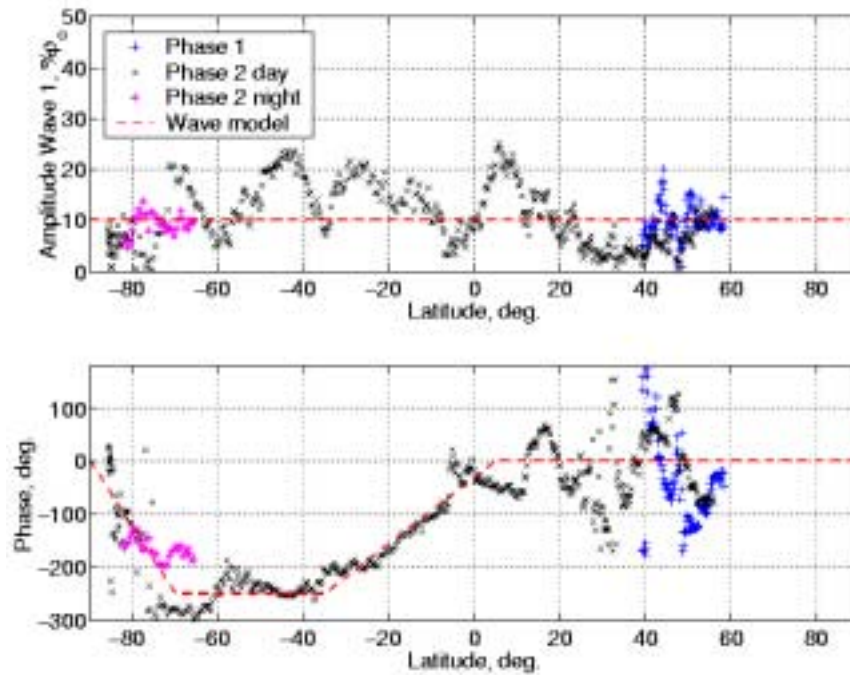


Figure B1. Wave 1 amplitude and phase.

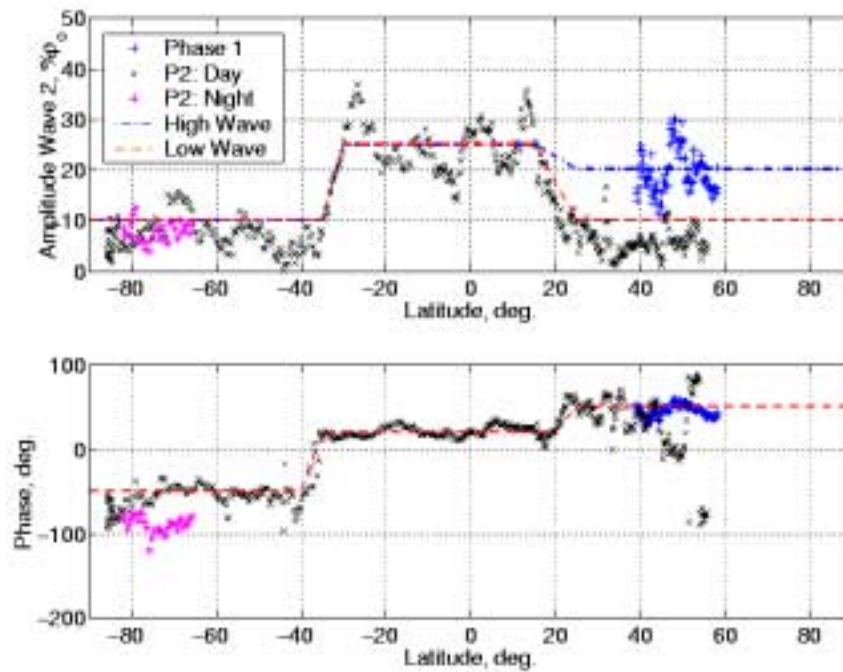


Figure B2. Wave 2 amplitude and phase.

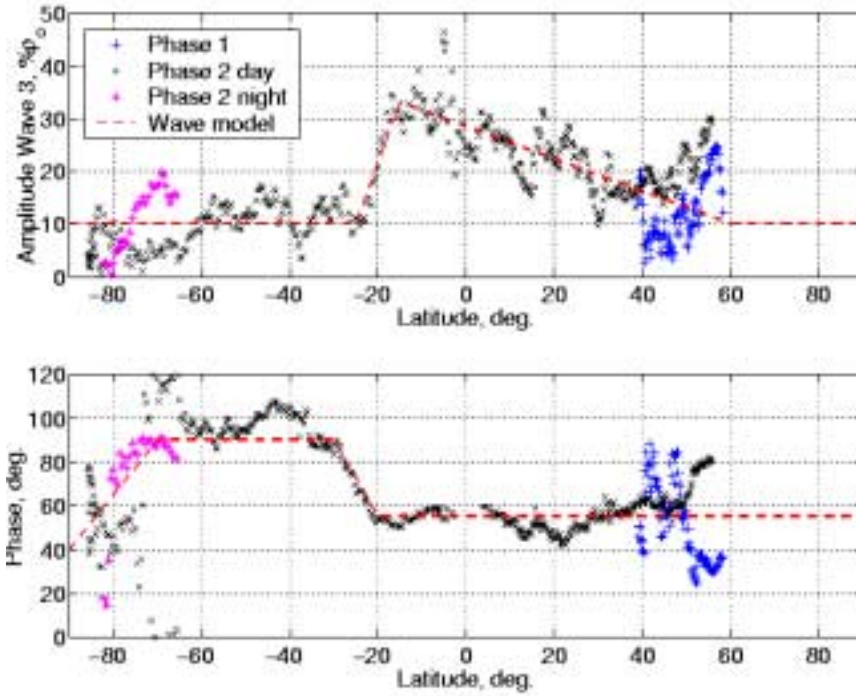


Figure B3. Wave 3 amplitude and phase.

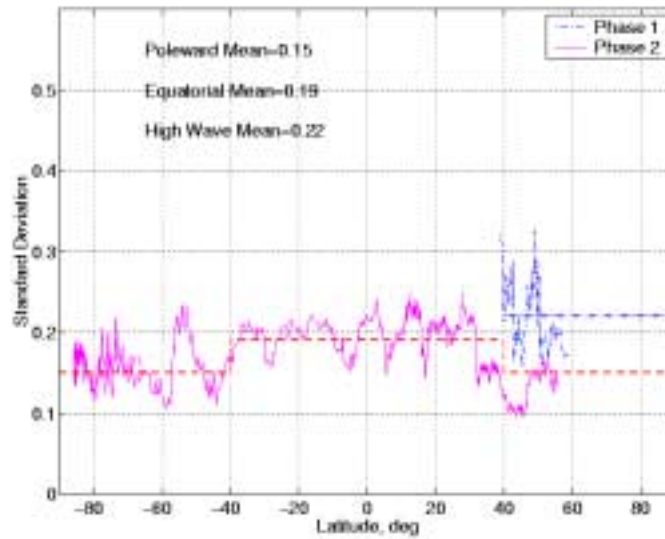


Figure B4. Standard deviation of the residuals for wave model solution.